

CrossMark  
click for updatesCite this: *Soft Matter*, 2015, 11, 2387

## Organelle morphogenesis by active membrane remodeling†

N. Ramakrishnan,<sup>ab</sup> John H. Ipsen,<sup>c</sup> Madan Rao<sup>de</sup> and P. B. Sunil Kumar<sup>\*a</sup>

Intracellular organelles are subject to a steady flux of lipids and proteins through active, energy consuming transport processes. Active fission and fusion are promoted by GTPases, *e.g.*, Arf–Coatamer and the Rab–Snare complexes, which both sense and generate local membrane curvature. Here we investigate, through Dynamical Triangulation Monte Carlo simulations, the role that these active processes play in determining the morphology and composition segregation in closed membranes. We find that the steady state shapes obtained as a result of such active processes, bear a striking resemblance to the ramified morphologies of organelles *in vivo*, pointing to the relevance of nonequilibrium fission–fusion in organelle morphogenesis.

Received 21st October 2014

Accepted 1st February 2015

DOI: 10.1039/c4sm02311k

www.rsc.org/softmatter

A characteristic feature of eukaryotic cells is the variety of membrane bound organelles, distinguished by their unique morphology and chemical composition. These internal organelles emerge in the face of a steady flux of material (lipids/proteins) in the form of membrane bound vesicles which fuse into and fission off from them. A central issue in cell biology is to explain the morphology of organelles as a consequence of the molecular processes and physical forces involved in this transport.<sup>1–3</sup> While there is detailed knowledge of the molecular processes involved in membrane remodeling at short scales, our understanding of the underlying physical principles governing large scale morphogenesis is still rudimentary.<sup>4</sup>

A possible indication of these underlying principles might be obtained by noting that despite the differences in membrane composition across organelles, ramified, tubular or sheet-like shapes are generic large scale morphologies observed in internal membranes, both in the secretory (*e.g.*, Golgi) and the endocytic (*e.g.*, endosomes) pathways, suggesting the involvement of common features shared by these organelles.

The most striking common aspect of organelles in the trafficking pathways is that they are dynamic membranous structures, subject to and driven by a continuous flux of a membrane bound material.<sup>5</sup> Several studies have shown that the time

scales of material flux *via* vesicle fission and fusion onto a compartment<sup>6</sup> are at least comparable to membrane relaxation times, which for a micron sized compartment, in the highly viscous environment of the cell,<sup>7</sup> is of the order of tens of seconds. The large scale morphology of the membrane bound compartments could be influenced by the active out-of-equilibrium processes of fission and fusion of material.

The other common aspect is that organelles are subject to the action of curvature sensing and curvature generating proteins which modulate the local membrane shape—such proteins now include a variety of bar-domain proteins,<sup>8</sup> coat-proteins<sup>9</sup> and GTPases<sup>10–13</sup> and are found on most membrane bound organelles and the plasma membrane. In particular, protein complexes such as Rabs–Snare and the Arf–Coatamer that promote fusion and fission, respectively,<sup>14</sup> shuttle between membrane bound and unbound states. The mechanochemistry of these bound complexes suggest that they respond to and drive changes in the local curvature of the membrane upon energy consumption,<sup>15</sup> see Fig. 1 for a schematic.

In this manuscript, we take these two common features, namely nonequilibrium fission–fusion affected by curvature generating proteins, as the primary driver of the membrane shape in internal organelles in the trafficking pathway. Our coarse-grained modeling approach incorporates the basic elements of transport and membrane physics, with minimal molecular detail. This is definitely an oversimplification, and we will not be able to comment on the shapes of specific organelles, which might require the addition of specific molecular aspects<sup>13,16</sup> on top of this basic common model. We hope, however, to capture the broad features of organelle morphogenesis by our model.

In general, the stochastic fission–fusion of vesicles from onto the organelle membrane, produce changes in both the local membrane curvature and membrane area.<sup>17–21</sup> In this

<sup>a</sup>Department of Physics, Indian Institute of Technology Madras, Chennai 600036, India. E-mail: sunil@physics.iitm.ac.in

<sup>b</sup>Department of Bioengineering, University of Pennsylvania, PA-19014, USA. E-mail: ramn@seas.upenn.edu

<sup>c</sup>MEMPHYS – Center for Biomembrane Physics, University of Southern Denmark, Odense, DK-5230, Denmark. E-mail: ipsen@memphys.sdu.dk

<sup>d</sup>Raman Research Institute, Bengaluru 560080, India

<sup>e</sup>National Centre for Biological Sciences (TIFR), Bengaluru 560065, India. E-mail: madan@ncbs.res.in

† Electronic supplementary information (ESI) available. See DOI: 10.1039/c4sm02311k

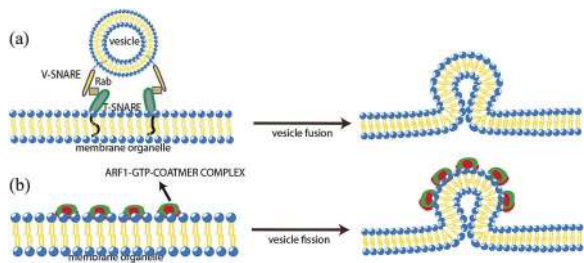


Fig. 1 Schematics of active fusion–fission mediated curvature changes. (a) Fusion of transport vesicle onto the organelle membrane is induced by the energy consuming Rab–Snare complex and accompanied by membrane deformation. (b) Fission of transport vesicle from the organelle membrane is induced by the energy consuming Arf–Coat complex and accompanied by membrane deformation. Our study extends to other active membrane processes, such as the switching of membrane bound pumps from their active to inactive forms (ESI Fig. S1†).

manuscript, for simplicity, we consider a perfectly balanced membrane where the rates of fission and fusion are the same. In this limit, there are no fluctuations in the lipid number. We study the morphological changes in a closed membrane induced by active curvature fluctuations arising from fission–fusion, using a Dynamic Triangulation Monte Carlo (DTMC) simulation. This ignores the effects of hydrodynamics and treats the membrane within a Rouse description. We display the steady state membrane shapes as a function of activity rate and the extent of curvature generation per active event and show how membrane activity manifests as a dynamical pressure. We conclude with a discussion on the significance of such actively driven membrane remodeling in describing the shapes of intracellular membrane organelles *in vivo*.

## 1 Model

Since we are interested in shape changes of a closed membrane over large spatiotemporal scales (size of organelle,  $10\ \mu\text{m} \gg$  size of transport vesicle,  $100\ \text{nm}$ ; membrane relaxation time scales,  $1\text{--}10\ \text{s} \gg$  inverse rate of material flux), it is appropriate to use a coarse-grained dynamical description of the membrane, governed by membrane elasticity, relaxational dynamics and activity.

### Membrane elasticity

To be able to describe the ramified, strongly non-axisymmetric shapes of membrane organelles, we use computer simulations, where the fluid membrane is represented as a triangulated closed surface with  $N$  vertices, denoted by  $\{\vec{X}\}$ , that are interconnected to form a triangulation map,  $\{\mathcal{T}\}$ , consisting of  $T$  triangles and  $L$  links (see ESI section S2† for a detailed description).

The membrane is assumed to be tensionless and in the absence of any activity, the elastic stresses can be described by the standard Canham–Helfrich energy functional,<sup>22,23</sup> whose discrete form is given by,

$$\mathcal{H}_{\text{el}} = \frac{\kappa}{2} \sum_{i=1}^N (H_i - H_{0i})^2 A_i - \Delta p_0 V, \quad (1)$$

where  $A_i$  is the area element associated with vertex  $i$ ,  $H_i$  is the local mean curvature and  $\kappa$  is the bending modulus, a material parameter taken to be uniform for simplicity. The local spontaneous curvature  $H_{0i}$ , whose form we declare later, is a measure of the preferred local mean curvature of the membrane and is non-zero only at the sites of activity. In addition, there is an osmotic pressure difference  $\Delta p_0$  which sets the scale of the mean enclosed volume at equilibrium.

Such simulation models have been used to study non-axisymmetric, multicomponent membranes, both at equilibrium and when subject to nonequilibrium driving.<sup>24–27</sup>

### Active fission–fusion induced by curvature generating/sensing proteins

The active events of fission and fusion are driven by curvature generating vesicle–protein complexes (Fig. 1), represented by a scalar field  $\phi$  at every vertex  $i$ , and takes values  $+1$  or  $-1$ , depending on whether this complex is bound to the membrane at  $i$  or not. When bound,  $\phi_i = 1$ , the complex induces a local spontaneous curvature at  $i$ , else it does not; this is achieved by setting  $H_{0i} = C_0(1 + \phi_i)/2$  in eqn (1).

At every vertex  $i$ , the transition probabilities for  $\phi_i \rightleftharpoons -\phi_i$  are taken to be independent of each other. We denote the mean attempt rate for these non-equilibrium curvature changes by  $\varepsilon$ , and choose a form of these transition rates,<sup>28</sup> so as to ensure that  $N_{\pm}$ , the instantaneous number of vertices with  $\phi_i = \pm 1$  (with  $N = N_+ + N_-$ ), does not deviate significantly from a desired value  $N_{\pm}^0$ . The explicit form of these transition rates are

$$\mathcal{P}_{+ \rightarrow -} = \varepsilon_- \left( \frac{N_+}{N} \right) \frac{1}{1 + \exp(\zeta[N_+ - N_- - A_0])} \quad (2)$$

and

$$\mathcal{P}_{- \rightarrow +} = \varepsilon_+ \left( \frac{N_-}{N} \right) \frac{1}{\eta + \exp(-\zeta[N_+ - N_- - A_0])}. \quad (3)$$

These transition rates are entirely dependent on the preferred asymmetry parameter,  $A_0 \equiv N_+^0 - N_-^0$ , and the parameter  $\zeta$  sets the scale of fluctuations in  $N_+$ .  $N_+^0$  and  $N_-^0$  denote the steady state mean values of  $N_+$  and  $N_-$ ; we ensure that  $N_{\pm}$  reaches  $N_{\pm}^0$  by setting  $\eta = \left( 2 \frac{N_-}{N_+} - 1 \right)$  in (3). Note that the above transition probabilities do not depend on the energy change associated with a change in local configuration,  $\phi \rightleftharpoons -\phi$ . This is unlike what one would expect for transition probabilities obeying detailed balance.

The adsorption–desorption of protein complexes and the concomitant membrane shape changes are non-equilibrium processes. The transition probabilities associated with these state changes explicitly break detailed balance, seen here as a violation of the Kolmogorov loop condition (ESI section S3†)—we show that there exists a loop in configuration space where the product of transition probabilities in one direction is not equal to the product

taken in the reverse direction. Detailed balance is restored when we set  $\varepsilon = 0$  or  $C_0 = 0$ . We will refer to  $\varepsilon$  as the activity rate, and  $C_0$ , as the curvature–activity coupling. On top of all this, we allow the curvature generation resulting from the binding and unbinding of these complexes to be cooperative, this could be accounted for by an Ising–Hamiltonian,

$$\mathcal{H}_\phi = -\frac{1}{2} \sum_{i=1}^N \sum_{j \in \Omega_i} J_{ij} \phi_i \phi_j, \quad (4)$$

where the summation is over sites  $j \in \Omega_i$ , the set of all vertices connected to  $i$ . While in principle  $J_{ij}$  can depend on the local curvature, for simplicity we take it to be homogeneous and equal to  $J$ . Note that  $J$  could be zero (uncorrelated (un)binding) or can have either sign; the existence of export sites<sup>29,30</sup> in the secretory system might suggest that  $J > 0$ .

### Monte Carlo dynamics of the membrane

The full Monte Carlo dynamics includes the above mentioned active processes, the usual Kawasaki exchange moves of the field  $\phi$ , and the Metropolis moves of membrane shape,<sup>25,31</sup> using the full Hamiltonian

$$\mathcal{H} = \mathcal{H}_{el} + \mathcal{H}_\phi, \quad (5)$$

as summarized in Fig. 2. It should be noted that unlike the active process which changes the value of  $\phi$  in a non-conserved manner, the Kawasaki exchange moves facilitate aggregation of  $\phi$  while keeping its average at a constant value, thereby taking the  $\phi$  distribution towards equilibrium. We define a Monte Carlo sweep (MCS) to be  $L$  attempts to flip links,  $N$  attempts to move vertices,  $N_+$

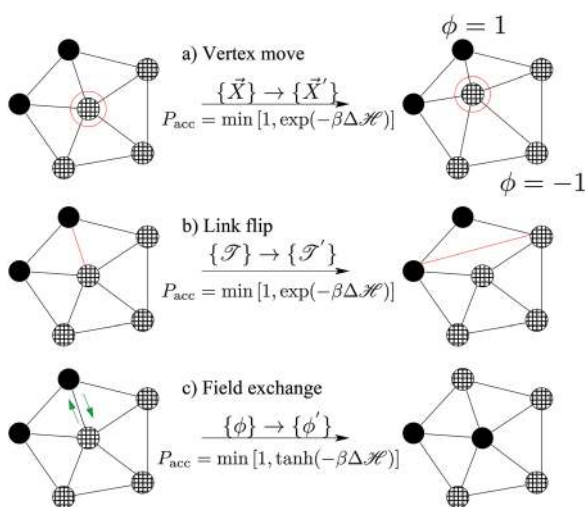


Fig. 2 DTMC of two-component fluid membranes. (a) A chosen vertex is randomly displaced in 3-dimensions keeping the connectivity  $\{\mathcal{T}\}$  unchanged. (b) A link is flipped (red line) to change connectivity. (c) Kawasaki exchange of  $\{\phi\}$  (green arrows) to enable diffusion of the active protein complex on the surface (see text for notation). Here  $\beta \equiv 1/k_B T$  ( $k_B$  is the Boltzmann constant and  $T$  is the temperature) and  $\Delta\mathcal{H}$  is the change in  $\mathcal{H}$  (eqn (5)) upon change in the conformational state of the membrane. In addition to the above moves, we carry out the active  $\phi \rightleftharpoons -\phi$  transitions at a rate set by  $\varepsilon$ .

attempts to exchange  $\phi_i$  with neighbouring vertices, and  $\varepsilon$  attempts to flip the value of  $\phi$  at vertices—this sets the unit of time.

We fix  $N_+^0 = 0.1N$  and vary  $\varepsilon$ ,  $C_0$  and  $J$  to explore the morphology of membranes at the nonequilibrium steady state.  $\kappa$  and  $J$  are in units of  $k_B T$ , and  $C_0$  is in units of  $a_0^{-1}$ , where  $a_0$  is the size associated with the coarse-grained vertices. Before discussing the results of the active membrane, we display the equilibrium membrane shapes and phase diagram by setting  $\varepsilon = 0$ , for different values of  $C_0$  and  $J$  in ESI Fig. S4.†

## 2 Results and discussion

Motivated by the phenomenology of trafficking dynamics in the secretory pathway,<sup>6</sup> we have explored the strong nonequilibrium regime where membrane relaxation times are longer than the timescale of activity. We monitor the time series of the volume, cluster number and mean elastic energy and show that they saturate to a nonequilibrium steady state.

The steady state morphologies of an active membrane are shown in Fig. 3. These shapes can be broadly classified as: (a) quasi-spherical, (b) prolate ellipsoids, (c) tubules and flattened sacs, and (d) stomatocytes. Fig. 4 shows the phase diagram of an active membrane in the  $\varepsilon$ – $C_0$  plane, with  $J$  fixed. Similarly, the phase diagram in the  $\varepsilon$ – $J$  plane for a fixed value of  $C_0$  is shown in

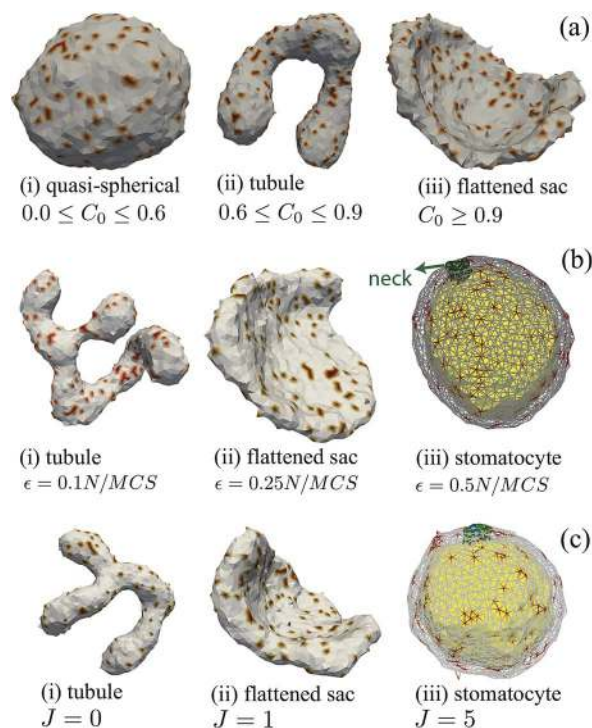


Fig. 3 Shapes of an active membrane. (a) Steady state shapes at  $\varepsilon = 0.1N/MCS$  and  $J = 0$ , as a function of curvature–activity coupling,  $C_0$ . (b) Steady state shapes at  $J = 0$  and  $C_0 = 0.8$ , as a function of activity rate,  $\varepsilon$ . The side of the stomatocyte that is curved-in, is colored differently, for clarity. (c) Steady state shapes at  $\varepsilon = 0.1N/MCS$  and  $C_0 = 0.8$ , as a function of cooperativity  $J$  between active species. All configurations are obtained with  $\kappa = 20$ ,  $\Delta p_0 = 0$  and  $N_+^0 = 0.1N$ . The locations of the active protein complexes are shown by the shaded regions.

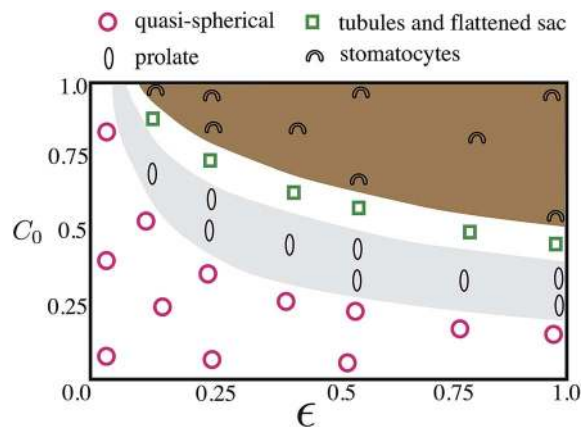


Fig. 4 Phases of the active closed membrane as a function of  $C_0$  and activity  $\epsilon$ . The phase boundaries are mere guides to the eyes, determined by visual inspection of the dominant shape within an ensemble of morphologies simulated at each state point.

Fig. 5. We now make detailed comments on the effect that each of these parameters have on the membrane shape. We study the steady state phase diagram of an active membrane upon varying  $C_0$ ,  $\epsilon$  and  $J$ .

#### Effect of curvature–activity coupling, $C_0$

Fig. 3a(i–iii) show a sequence of steady state shapes of the active membrane going from quasi-spherical to tubule to flattened sac on increasing  $C_0$ , at a fixed activity rate  $\epsilon = 0.1N/\text{MCS}$ . These nonequilibrium steady state shapes are distinct from their equilibrium counterparts (ESI Fig. S4<sup>†</sup>), obtained when the activity rate  $\epsilon = 0$ .

#### Effect of activity rate, $\epsilon$

The steady state shapes are very sensitive to the rates of activity and go from tubular to flattened sacs to stomatocyte as the

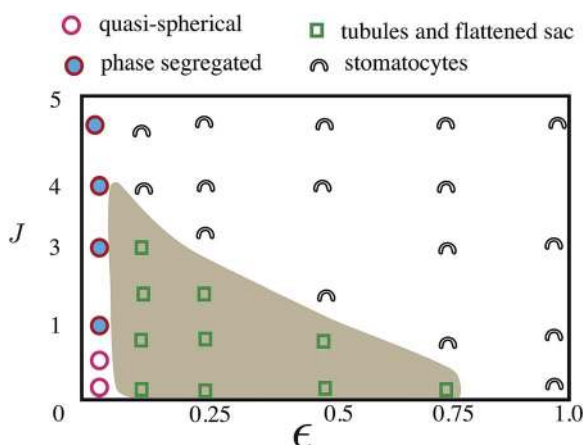


Fig. 5 Phase diagram of the closed active membrane as a function of  $J$  and activity  $\epsilon$ , for a fixed  $C_0 = 0.8$ . The phase boundaries are mere guides to the eyes, determined by visual inspection of the dominant shape within an ensemble of morphologies simulated at each state point. Appreciable phase-segregation of the protein species happens only in the absence of activity,  $\epsilon = 0$ , and when  $J \approx 1$ .

activity rate is increased. This is illustrated in Fig. 3b for three activity rates,  $\epsilon = 0.1, 0.25$  and  $0.5N/\text{MCS}$ , at a fixed value of  $C_0 = 0.8$ .

#### Effect of cooperativity, $J$

Cooperativity between the active species,  $J > 0$ , promotes the formation of clusters, which in turn enhances the effects of activity and curvature–activity coupling, consistent with the results reported in ref. 32 for the case of membrane mediated aggregation of active pumps, and leads to the sequence of shapes depicted in Fig. 3c. We find that while activity promotes small clusters, it prevents the formation of larger clusters (Fig. 6a).

This point deserves further discussion. For an equilibrium membrane, the critical transition to having large clusters occurs around  $J \sim 1$  (Fig. 6b), with the size of the largest cluster scaling with the total number of aggregating particles. In contrast, for the active membrane with  $\epsilon = 0.1$ , there is no large scale cluster formation at the steady state—indeed, though the average domain size increases with  $J$ , 70% of the active species are still monomeric (Fig. 6a).

We compute the cluster size distribution  $P(s)$ , and find that it fits to a power law, with an exponential cutoff:  $P(s) \sim s^{-\alpha} \exp(-s/s_0)$ , with the exponent  $\alpha$  and  $s_0$  roughly independent of  $\epsilon$ , but dependent on  $J$  (Fig. 6 and ESI section S6<sup>†</sup>). The exponent  $\alpha \approx 1$ , for small values of  $J$ , is consistent with the results of Turner *et al.*<sup>15</sup>

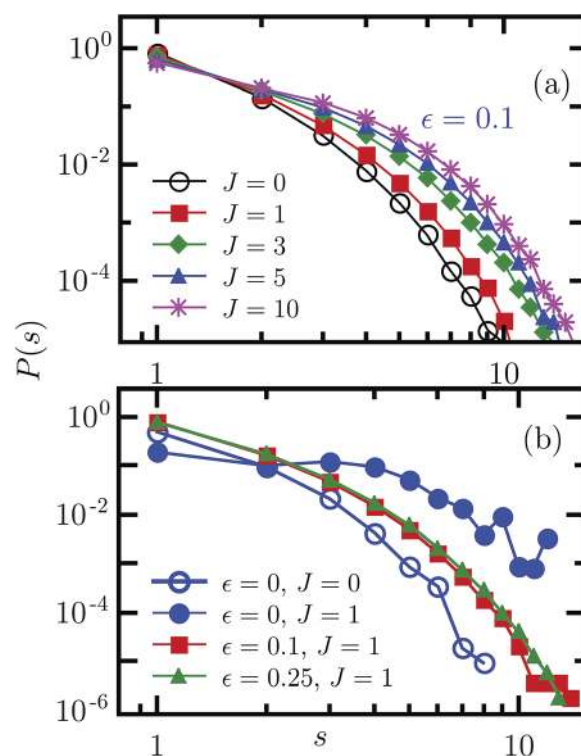


Fig. 6 Normalized cluster size distribution  $P(s)$  of the active species (a) as a function of  $J$  at  $\epsilon = 0.1N/\text{MCS}$ , (b) as a function of activity rate,  $\epsilon$ , given in units of  $N/\text{MCS}$ . The equilibrium distribution ( $\epsilon = 0$ ) for  $J = 0$  and 1 is shown for comparison. Here,  $N_+^0 = 0.1N$  and  $C_0 = 0.8$ .

The phase diagram of the steady state morphologies of an active membrane in  $\varepsilon$ - $C_0$  and  $\varepsilon$ - $J$  space, displayed in Fig. 4 and 5, shows that the same ramified or flattened shape can be achieved either by increasing  $\varepsilon$  or  $C_0$ . To identify order parameters characterizing these phases, we first note that the surface area of the active membrane remains roughly constant (Fig. 7), not surprising given that the DTMC moves do not allow for a change in the total number of vertices  $N$  and are connected by tethers. We therefore characterize these phase transitions by geometrical order parameters such as the scaled volume  $V/V_0$ , where  $V_0$  is the volume of the fully inflated sphere, or the ratio of the surface area-to-volume.

The scaled volume, collapses abruptly as the membrane shape transforms from a quasi-spherical conformation to a tubule or a disc, and thereafter smoothly goes to zero as the membrane transforms to a stomatocyte (Fig. 8). This transition is also evident in the behaviour of other geometrical measures related to the gyration tensor, such as asphericity and shape-anisotropy (ESI section S9†). This collapse transition is of purely non-equilibrium origin, its onset is advanced when  $\varepsilon$  increases and is absent for an equilibrium membrane,  $\varepsilon = 0$  (Fig. 8).

Thus far, we had not imposed any constraint on the volume enclosed by the membrane, which allows the quasi-spherical membrane at equilibrium to acquire volume  $V$  such that the membrane tension and excess pressure are zero. It should be

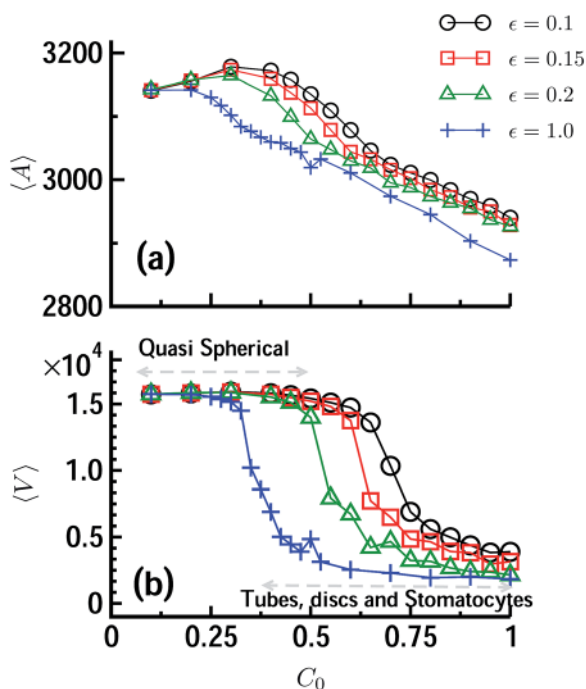


Fig. 7 (a) The average membrane area remains roughly the same (within a range permissible by the tight bounds on the tether lengths), upon changes in  $C_0$  and  $\varepsilon$ . (b) Average volume  $\langle V \rangle$  enclosed as function of  $C_0$  for different values of  $\varepsilon$  shows significant changes. The transition from a quasi-spherical membrane to tubular/flattened sacs/stomatocytes is accompanied by a sharp reduction in the enclosed volume. Here,  $\kappa = 20$ ,  $C_0 = 0.8$ ,  $J = 0$  and  $N_+^0 = 0.1N$ .

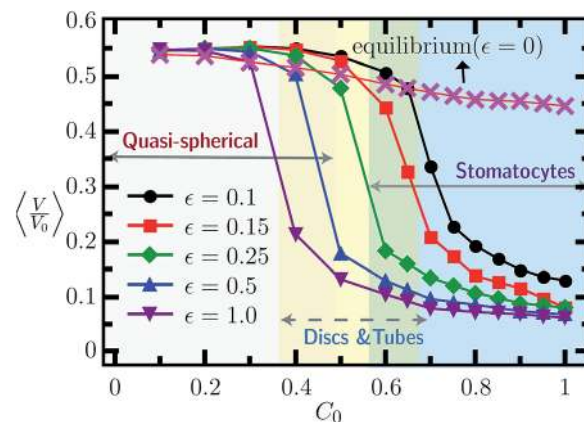


Fig. 8 Scaled enclosed volume  $\langle V/V_0 \rangle$  as a function of  $C_0$  with  $\kappa = 20$ ,  $J = 0.0$  and  $N_+^0 = 0.1N$  for different values of  $\varepsilon$  in units of  $N/\text{MCS}$ . The transition from quasi-spherical to tube, disc and stomatocyte is shown by the various shaded regions for the specific case of  $\varepsilon = 0.1N/\text{MCS}$ . The transition from a quasi-spherical vesicle to other shapes is characterized by a jump in the enclosed volume and gets sharper as  $\varepsilon$  increases. The equilibrium,  $\varepsilon = 0$ , curve is when 10% of the vertices have a local spontaneous curvature  $C_0$ .

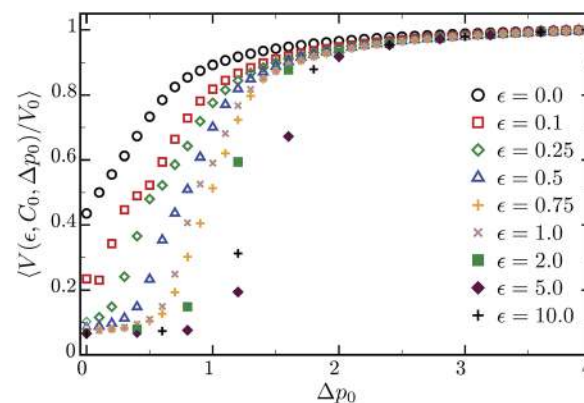


Fig. 9 Volume as a function of the bare pressure  $\Delta p_0$ , for an active membrane with  $C_0 = 0.8$  and for activity rates  $\varepsilon = 0.0, 0.1, 0.25, 0.5, 0.75, 1.0, 2.0, 5.0$  and  $10.1N/\text{MCS}$ .

noted that the resulting enclosed volume  $V \leq V_0$ , where  $V_0$  is the volume enclosed by the membrane, with the same  $N$  vertices, when it is fully inflated. Starting from this equilibrium state with  $V/V_0 < 1$  and  $C_0 = 0$ , we now explore the steady state shapes, at different activity rates, as a function of an added pressure  $\Delta p_0$  (Fig. 9). At large positive  $\Delta p_0$ , the membrane is an inflated sphere. The pressure required to fully inflate the membrane increases with  $C_0$  and activity rate  $\varepsilon$ . On plotting the scaled volume versus an activity renormalized pressure  $\Delta p = \Delta p_0 + \Delta p_a$ , we find a complete data collapse (Fig. 10).  $\Delta p_a$  is an activity induced dynamical pressure, whose sign is negative. This dynamic pressure is calculated as follows. Starting from a fully inflated equilibrium vesicle with volume  $V_0$ , which will now have tension  $\sigma_0$ , we obtain the steady state configuration of the vesicle for a fixed activity rate and  $C_0$ . The enclosed volume  $V$  at the steady state is a decreasing function of  $\varepsilon$  and  $C_0$ , as shown in Fig. 7.

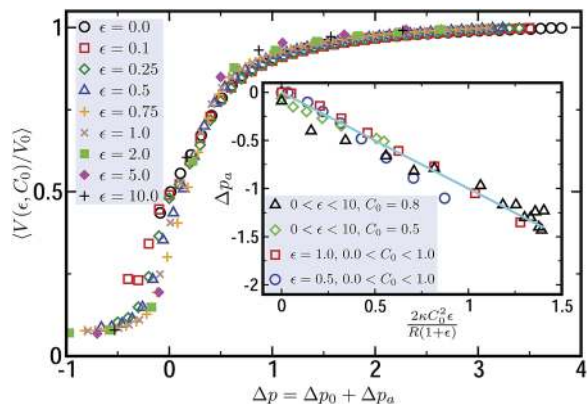


Fig. 10 Data collapse of the scaled enclosed volume versus the activity renormalized pressure,  $\Delta p$ . Data correspond to  $\kappa = 20$ ,  $C_0 = 0.8$ ,  $N_+^0 = 0.1N$  with  $\varepsilon = 0.0, 0.1, 0.25, 0.5, 0.75, 1.0, 2.0, 5.0$  and  $10.1N/MCS$ . (Inset) Computed values of the dynamic pressure  $\Delta p_a$  for different values of  $\varepsilon$  and  $C_0$  shows a good fit to  $2\varepsilon\kappa C_0^2/R(1 + \varepsilon)$ , where  $R = 19.4a_0$  is the radius of the fully inflated membrane.

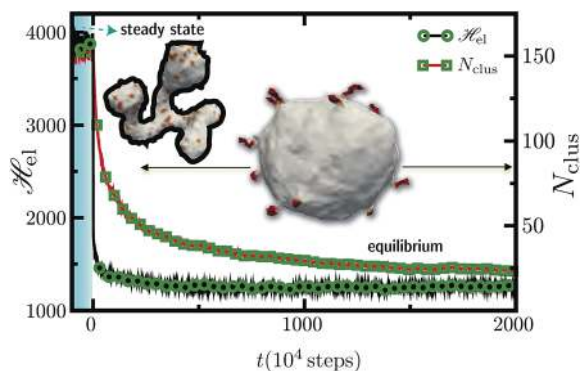


Fig. 11 Time evolution of an active tubular membrane at steady state, with  $C_0 = 0.8$ ,  $\kappa = 20$ ,  $N_+^0 = 0.1N$ ,  $J = 1$ , and  $\varepsilon = 0.1N/MCS$ , following the inhibition of activity—the time axis has been shifted such that the inhibition occurs at  $t = 0$ . The membrane relaxes to equilibrium, forming buds, characteristic of two-component membranes,<sup>25</sup> in the process of minimizing the elastic energy,  $\mathcal{H}_{el}$  (open circles). Concomitantly, domains, enriched in the protein complex, coarsen resulting in a monotonic reduction of the cluster number,  $N_{clus}$  (open squares). Symbols have been shown only at some representative points.

Starting from the steady state of the active membrane obtained for every pair of  $\varepsilon$  and  $C_0$ , an inflating pressure  $\Delta p_0$  is applied in small increments and the individual  $\Delta p_0$ - $V$  isotherms are recorded until the active membrane becomes fully inflated, *i.e.* until  $V(\varepsilon, C_0, \Delta p_0)/V_0 \sim 1$ . The isotherms for an active membrane (see Fig. 9) for the case of  $C_0 = 0.8$  show a modified behaviour when compared to the isotherm obtained at equilibrium. We find that the maximum pressure required to inflate the vesicle increases by a value  $\Delta p_a$ , whose origin is dynamic, and is dependent on both  $\varepsilon$  and  $C_0$ . The isotherms for the active membrane collapse onto the equilibrium curve, as shown in Fig. 10, when the bare osmotic pressure  $\Delta p_0$  is rescaled by the corresponding dynamical pressure  $\Delta p_a$  to obtain an effective pressure  $\Delta p = \Delta p_0 + \Delta p_a$ .

To obtain an analytic estimate of the dynamical pressure  $\Delta p_a$ , we generalize the condition for equilibrium of an inflated spherical membrane<sup>33</sup> to this active case:  $\Delta p_0 R + 2(\sigma_0 + \sigma_a) - \kappa C_0^2 = 0$ , where  $R$  is the radius of the inflated sphere,  $\sigma_0$  is the tension on the equilibrium fully inflated membrane, and  $\sigma_a = -\varepsilon\kappa C_0^2/(1 + \varepsilon)$  is the dynamic tension induced by fission–fusion at an activity rate  $\varepsilon$ .<sup>‡</sup> This dynamic tension can be reinterpreted as a renormalized pressure,  $\Delta p = \Delta p_0 - 2\varepsilon\kappa C_0^2/R(1 + \varepsilon)$ , consistent with the demonstration in the inset of Fig. 10.

### 3 Concluding remarks

Our goal here has been to be able to describe generic large scale morphologies, such as ramified, tubular or sheet-like shapes, that seem to be shared by many different internal membrane compartments, both in the secretory (*e.g.*, Golgi) and the endocytic (*e.g.*, endosomes) pathways, using a common shared dynamical feature, namely the non-equilibrium processes of fission–fusion driven using energy consuming mechano-chemical transducers.

This places nonequilibrium phenomena at the heart of organelle morphogenesis and appears to have some level of support.<sup>1,34,35</sup> Our work should not be viewed as being inconsistent with the view that tubular and flat organelle morphologies can arise from forces generated by specialized curvature-modifying proteins or protein scaffolding proteins.<sup>4,13,36–41</sup> It could be that tubular and flattened sheet-like structures formed as a result of active fission–fusion are stabilized by the presence of protein scaffolds. In addition, it is possible that the presence of filamentous cytoskeletal structures could provide a scaffold that directly affects the membrane shape.

How does one experimentally test this nonequilibrium perspective? The definitive aspects of the active nonequilibrium viewpoint will be manifested in the dynamical fluctuations at the steady state, the dynamical response to perturbations and the dynamics towards the steady state.<sup>17,18</sup> Unfortunately, these aspects cannot be analyzed using Monte Carlo simulations. A simple and unique consequence of the active driving would be the centre-of-mass movement of the entire organelle when the flux of activity breaks fore-aft symmetry, and could in principle be amenable to experiments. Similarly, other consequences, such as spontaneous swelling and tubular instabilities due to activity induced negative tension,<sup>17,21,42</sup> arise when there is an imbalance between fission–fusion dynamics.

Fig. 11 demonstrates how the shape and composition of the active membrane relaxes towards equilibrium when the activity  $\varepsilon$  is abruptly shut off. Starting from an initial tubular morphology of the active membrane, the shape changes rapidly to give rise to an inflated, near-spherical equilibrium morphology. The elastic energy  $\mathcal{H}_{el}$  drops exponentially fast and that the curvature sensing/generating proteins cluster and coarsen, as indicated by a rapid decrease of  $N_{clus}$ , to form tubular buds (as in Kumar *et al.*<sup>25</sup>). This shape evolution is

<sup>‡</sup> An induced tension of a similar form was proposed recently for an equilibrium membrane when it is constrained to a configuration with curvature less than the one set by the spontaneous curvature: R. Lipowsky, *Faraday Disc.*, 2013, **161**, 305.

shown in ESI Movies M1 and M2.† Experimental approaches, in which one monitors the dynamics of shape changes of Golgi compartments using high resolution live-cell imaging, when the agencies of active fission and fusion are suddenly switched off, could help resolve these issues.

Admittedly, one cannot ignore the effects of both specific curvature generating proteins or the cytoskeletal scaffolding on shaping the membrane conformations. In future, we plan to add these effects to the nonequilibrium framework presented here. We hope the results obtained here will drive further experimental efforts in arriving at a deeper understanding of the fundamental issues governing organelle morphogenesis.

## References

- 1 S. M. Rafelski and W. F. Marshall, *Nature*, 2008, **9**, 593–602.
- 2 W. F. Marshall, *BMC Biol.*, 2011, **9**, 57.
- 3 J. A. Martínez-Menárguez, *ISRN Cell Biol.*, 2013, **2013**, 1–15.
- 4 Y. Shibata, J. Hu, M. M. Kozlov and T. A. Rapoport, *Annu. Rev. Cell Dev. Biol.*, 2009, **25**, 329–354.
- 5 B. Alberts, A. Johnson, J. Lewis, M. Raff, K. Roberts and P. Walter, *Molecular Biology of the Cell*, Garland Publishing, Singapore, 3rd edn, 1994.
- 6 F. T. Wieland, M. L. Gleason, T. A. Serafini and J. E. Rothman, *Cell*, 1987, **50**, 289–300.
- 7 D. Wirtz, *Annu. Rev. Biophys.*, 2009, **38**, 301–326.
- 8 A. Frost, V. M. Unger and P. De Camilli, *Cell*, 2009, **137**, 191–196.
- 9 C. D'Souza-Schorey and P. Chavrier, *Nature*, 2006, **7**, 347–358.
- 10 B. Marks, M. H. B. Stowell, Y. Vallis, I. G. Mills, A. Gibson, C. R. Hopkins and H. T. McMahon, *Nature*, 2001, **410**, 231–235.
- 11 F. Baschieri and H. Farhan, *Small GTPases*, 2012, **3**, 80–90.
- 12 K. P. Harris and J. T. Littleton, *Curr. Biol.*, 2011, **21**, R841–R843.
- 13 J. Zimmerberg and M. M. Kozlov, *Nature*, 2005, **7**, 9–19.
- 14 P. Chavrier and B. Goud, *Curr. Opin. Cell Biol.*, 1999, **11**, 466–475.
- 15 M. Turner, P. Sens and N. Socci, *Phys. Rev. Lett.*, 2005, **95**, 168301.
- 16 F. Campelo and M. M. Kozlov, *PLoS Comput. Biol.*, 2014, **10**, e1003556.
- 17 M. Rao and R. C. Sarasij, *Phys. Rev. Lett.*, 2001, **87**, 128101.
- 18 P. Girard, F. Jülicher and J. Prost, *Eur. Phys. J. E*, 2004, **14**, 387–394.
- 19 M. Klann, H. Koeppl and M. Reuss, *PLoS One*, 2012, **7**, e29645.
- 20 I. Ispolatov and A. Müsch, *PLoS Comput. Biol.*, 2013, **9**, e1003125.
- 21 M. Staykova, D. P. Holmes, C. Read and H. A. Stone, *Proc. Natl. Acad. Sci. U. S. A.*, 2011, **108**, 9084–9088.
- 22 P. B. Canham, *J. Theor. Biol.*, 1970, **26**, 61–81.
- 23 W. Helfrich, *Z. Naturforsch., C: Biochem., Biophys., Biol., Virol.*, 1973, **28**, 693–703.
- 24 G. Gompper and D. Kroll, *Phys. Rev. Lett.*, 1994, **73**, 2139–2142.
- 25 P. B. Sunil Kumar, G. Gompper and R. Lipowsky, *Phys. Rev. Lett.*, 2001, **86**, 3911–3914.
- 26 H. Noguchi and G. Gompper, *Proc. Natl. Acad. Sci. U. S. A.*, 2005, **102**, 14159–14164.
- 27 N. Ramakrishnan, P. B. Sunil Kumar and J. H. Ipsen, *Phys. Rev. E: Stat., Nonlinear, Soft Matter Phys.*, 2010, **81**, 041922.
- 28 W. Im, S. Seefeld and B. Roux, *Biophys. J.*, 2000, **79**, 788.
- 29 F. Brandizzi and C. Barlowe, *Nature*, 2013, **14**, 382–392.
- 30 A. Spang, *Cold Spring Harbor Perspect. Biol.*, 2013, **5**, a013391.
- 31 P. B. Sunil Kumar and M. Rao, *Phys. Rev. Lett.*, 1998, **80**, 2489–2492.
- 32 S. Ramaswamy, J. Toner and J. Prost, *Phys. Rev. Lett.*, 2000, **84**, 3494–3497.
- 33 U. Seifert, *Adv. Phys.*, 1997, **46**, 13–137.
- 34 Y.-H. M. Chan and W. F. Marshall, *Organogenesis*, 2010, **6**, 88–96.
- 35 Y. Shibata, T. Shemesh, W. A. Prinz, A. F. Palazzo, M. M. Kozlov and T. A. Rapoport, *Cell*, 2010, **143**, 774–788.
- 36 S. Leibler, *J. Phys.*, 1986, **47**, 507–516.
- 37 P. Sens, L. Johannes and P. Bassereau, *Curr. Opin. Cell Biol.*, 2008, **20**, 476–482.
- 38 J. Hu, Y. Shibata, C. Voss, T. Shemesh, Z. Li, M. Coughlin, M. M. Kozlov, T. A. Rapoport and W. A. Prinz, *Science*, 2008, **319**, 1247–1250.
- 39 N. Ramakrishnan, J. H. Ipsen and P. B. Sunil Kumar, *Soft Matter*, 2012, **8**, 3058.
- 40 M. Simunovic, C. Mim, T. C. Marlovits, G. Resch, V. M. Unger and G. A. Voth, *Biophys. J.*, 2013, **105**, 711–719.
- 41 M. M. Kozlov, F. Campelo, N. Liska, L. V. Chernomordik, S. J. Marrink and H. T. McMahon, *Curr. Opin. Cell Biol.*, 2014, **29**, 53–60.
- 42 J. Solon, J. Pécréaux, P. Girard, M.-C. Fauré, J. Prost and P. Bassereau, *Phys. Rev. Lett.*, 2006, **97**, 098103.